JGR Earth Surface

RESEARCH ARTICLE
10.1029/2023JF007177

Remote Sensing of Riverbank Migration Using Particle Image Velocimetry

Austin J. Chadwick[1], **Evan Greenberg**[1], **and Vamsi Ganti**[1,2]

[1]Department of Geography, University of California Santa Barbara, Santa Barbara, CA, USA, [2]Department of Earth Science, University of California Santa Barbara, Santa Barbara, CA, USA

Key Points:

- We upscale particle image velocimetry from laboratory studies to global remote sensing of riverbank migration
- Results are consistent with bank- and centerline-based methods and offer means to propagate uncertainty in channel position
- The method excludes cutoff and avulsion processes by design and targets channel migration regardless of planform morphology

Supporting Information:

Supporting Information may be found in the online version of this article.

Correspondence to:

A. J. Chadwick,
achadwick@ucsb.edu

Citation:

Chadwick, A. J., Greenberg, E., & Ganti, V. (2023). Remote sensing of riverbank migration using particle image velocimetry. *Journal of Geophysical Research: Earth Surface*, *128*, e2023JF007177. https://doi.org/10.1029/2023JF007177

Received 20 MAR 2023
Accepted 22 JUN 2023
Corrected 19 JUL 2023

This article was corrected on 19 JUL 2023. See the end of the full text for details.

Author Contributions:

Conceptualization: Austin J. Chadwick, Vamsi Ganti
Formal analysis: Austin J. Chadwick, Evan Greenberg, Vamsi Ganti
Funding acquisition: Vamsi Ganti
Investigation: Austin J. Chadwick, Vamsi Ganti
Methodology: Austin J. Chadwick, Evan Greenberg, Vamsi Ganti
Project Administration: Vamsi Ganti
Resources: Vamsi Ganti
Software: Austin J. Chadwick, Evan Greenberg
Supervision: Vamsi Ganti

Abstract Mobile river channels endanger human life and property and over centuries shape ecosystems, landscapes, and stratigraphy. Quantifying channel movements from remote sensing is difficult, in part due to the diversity of river mobility processes (e.g., channel migration, cutoffs, avulsion) and planform morphologies (e.g., meandering, braided). Here, we present a framework for quantifying riverbank migration from remote sensing that upscales recent methodological advances from laboratory flume studies utilizing particle image velocimetry (PIV). We apply PIV to image time series of 21 rivers worldwide, showing PIV ignores cutoff and avulsion processes by design and is well suited for tracking riverbank migration regardless of planform morphology. We show that PIV-derived results for riverbank migration are consistent with published results from centerline- and bank-based Lagrangian methods. Unlike existing methods, PIV offers a grid-based Eulerian framework where defining channel centerlines is unnecessary and quantified uncertainty in riverbank positions is propagated into uncertainty in migration rates. PIV offers means to efficiently extract global patterns in riverbank migration from decades of satellite data, as well as investigate river response to climate change and human activities in our rapidly changing world.

Plain Language Summary Roughly 3 billion people worldwide live along large rivers and rely upon them for food, water, transport, and energy. To ensure the safety and sustainability of riverside communities, it is important that we understand how rivers migrate over time. Satellite missions like NASA Landsat have captured millions of images of migrating rivers worldwide for more than thirty years—more images than can be feasibly mapped manually. Here, we build on previous work and present a method to automatically map riverbank migration from satellite images using a technique called particle image velocimetry (PIV). We apply PIV to Landsat-image time series for 21 example rivers and show that PIV results are efficient, reproducible, and accurate compared with existing automatic techniques. Importantly, unlike existing techniques, the PIV method directly accounts for the inherent uncertainty in migration-rate measurements that comes from trying to identify riverbanks from satellite imagery. Furthermore, PIV is equally applicable to all kinds of rivers (e.g., meandering, braided), opening up new opportunities to investigate the diversity of rivers and their responses to climate change and human activities.

1. Introduction

River channels are inherently mobile. Their movement across floodplains is responsible for shaping Earth's lowland ecosystems and landscapes (Paola et al., 1992; Ward & Stanford, 1995; Willenbring et al., 2013), constructing sedimentary stratigraphy (Chamberlin & Hajek, 2019; Ganti et al., 2020; Lynds & Hajek, 2006), and regulating the terrestrial organic carbon cycle (Douglas et al., 2021; Repasch et al., 2021; Scheingross et al., 2021; Torres et al., 2017). Over human lifetimes, channel movements endanger life and property on adjacent land (Church & Ferguson, 2015; Thakur et al., 2012) and shift the availability of water resources (Gleick, 2003; Passalacqua et al., 2021)—consequences linked to the displacement of millions of people over human history (Giosan et al., 2012; Kidder & Liu, 2017; Singh et al., 2017). To ensure the safety and sustainability of the 2.5+ billion people who live along river systems (Best, 2019), it is imperative we quantify and understand how river channels move.

Decades of imagery from remote sensing campaigns (e.g., NASA Landsat) capture diverse examples of channel mobility (Baki & Gan, 2012; Constantine et al., 2014; Gupta et al., 2013; Loveland & Dwyer, 2012; Schwenk et al., 2017; Sylvester et al., 2019). Channels move gradually through the process of riverbank migration (Einstein, 1926; Hickin & Nanson, 1984) and also in abrupt, periodic events such as cutoffs and avulsions

Validation: Austin J. Chadwick, Evan Greenberg, Vamsi Ganti
Visualization: Austin J. Chadwick, Evan Greenberg, Vamsi Ganti
Writing – original draft: Austin J. Chadwick, Vamsi Ganti
Writing – review & editing: Austin J. Chadwick, Evan Greenberg, Vamsi Ganti

that reroute the course of flow (Brooke et al., 2022; Constantine & Dunne, 2008; Hooke, 2004; Slingerland & Smith, 2004). Furthermore, channels exist across a continuum of different planform morphologies, from *single-thread* meandering channels (Figure 1a–1d) to *multi-thread* anabranching channels (Figures 1e–1g), which can be further categorized as braided, anastamosing, or wandering (Eaton et al., 2010; Galeazzi et al., 2021; Latrubesse, 2008). Manually mapping the wealth of remotely sensed channel motions is labor-intensive and inherently subjective, which has led to the development of automated methods (Dey & Bhattacharya, 2014; Dillabaugh et al., 2002; Jones, 2015, 2019; Marra et al., 2014; Rowland et al., 2016).

Automated methods commonly quantify channel migration based on the movement of the channel's centerline (Figure 2a). Centerlines are defined in each image and correlated through time using dynamic time warping (DTW) or similar nearest-neighbor algorithms (Lisiecki & Lisiecki, 2002; Rowland et al., 2016; Sylvester et al., 2019). Centerline-based methods have yielded numerous insights, especially for the migration of single-thread channels (Constantine et al., 2014; Sylvester et al., 2019). However, centerline-based methods are difficult to apply to multi-thread channels because centerlines of the interwoven channel threads are often ill-defined (Dey & Bhattacharya, 2014; Marra et al., 2014) (Figure 1e–1g). Furthermore, a centerline-based approach cannot capture the dynamics of opposing banks, which may accrete and erode at different speeds, especially over short timescales (~1–10 years) (Eke, Czapiga, et al., 2014; Mason & Mohrig, 2019).

To overcome the limitations of the centerline-based approach, newer automated methods have been developed based on tracking the channel's banks (Langhorst & Pavelsky, 2023; Nagel et al., 2022; Rowland et al., 2016). By tracking migration of the riverbank rather than the channel centerline, bank-based approaches are equally applicable to single- and multi-thread rivers and can capture differences in migration between opposing banks (Figure 2b). A prominent bank-based approach is Spatially Continuous Riverbank Erosion and Accretion Measurements (SCREAM) (Rowland et al., 2016). For input to SCREAM, each satellite image is converted into a binary mask representing either river or land, with banks defined by the interface. SCREAM then detects discrete areas that changed from land to river (erosion) or river to land (accretion) between masks. Linear rates of erosion/accretion are determined for each bank by the nearest-neighbor distance to bank pixels in the subsequent image within the same erosion/accretion area (Figure 2b) (Rowland et al., 2016). SCREAM and similar bank-based approaches have enabled researchers to quantify the mobility of both single- and multi-thread rivers in the Arctic (Douglas et al., 2021; Rowland et al., 2016, 2019) and beyond (Langhorst & Pavelsky, 2023; Nagel et al., 2022).

Importantly, past studies also highlight the difficulty of quantifying uncertainty within a bank-based approach. The identification of bank positions is typically the greatest source of uncertainty in remotely sensed riverbank-migration measurements (Donovan et al., 2019; Lane et al., 2010; Nagel et al., 2022), on account of pixel misclassifications; image resolutions; variations in river discharge; and user-end decisions to use either the edge of vegetation (Boruah et al., 2008; Donovan et al., 2019) or the edge of annual surface water (Lane et al., 2010; Langhorst & Pavelsky, 2023) as proxies for bank position. Quantifying these uncertainties and propagating them into migration measurements is inherently difficult in a bank-based approach because bank positions create the foundation of the Lagrangian (i.e., object-based) coordinate system (Figure 2b). Global uncertainties in bank-based measurements have been estimated by numerically simulating different sources of uncertainty and comparing simulated data to actual data (Langhorst & Pavelsky, 2023), but actual uncertainties associated with remotely sensed migration rates remain elusive.

Recent experimental advances have developed an alternative method for quantifying riverbank migration from plan-view imagery using particle image velocimetry (PIV) (Figure 2c) (Chadwick, Steel, Passalacqua, & Paola, 2022; Chadwick, Steel, Williams-Schaetzel, et al., 2022). Similar to bank-based approaches, PIV tracks the motion of channel banks (rather than centerlines) and is applicable to both single- and multi-thread channels (Figures 2b and 2c). PIV could also offer distinct advantages if upscaled from experimental to remote-sensing applications. Originally designed to track particles in a moving fluid, the PIV algorithm quantifies motion by correlating numerous sub-images on an Eulerian grid that is independent of the channel centerline or bank position (Figure 2c) (Keane & Adrian, 1992; Westerweel, 1997). This independence allows the uncertainty in bank positions to be quantified and then propagated into uncertainty in channel mobility (Chadwick, Steel, Williams-Schaetzel, et al., 2022). Furthermore, laboratory results demonstrate that the PIV algorithm specifically targets mobility associated with channel migration, and by design ignores mobility associated with cutoffs and avulsions (Chadwick, Steel, Williams-Schaetzel, et al., 2022)—events that typically need to be manually identified and removed in bank- and centerline-based approaches to avoid disruptions to the Lagrangian coordinate systems and nearest-neighbor algorithms (Rowland et al., 2016; Schwenk et al., 2017; Sylvester et al., 2019).

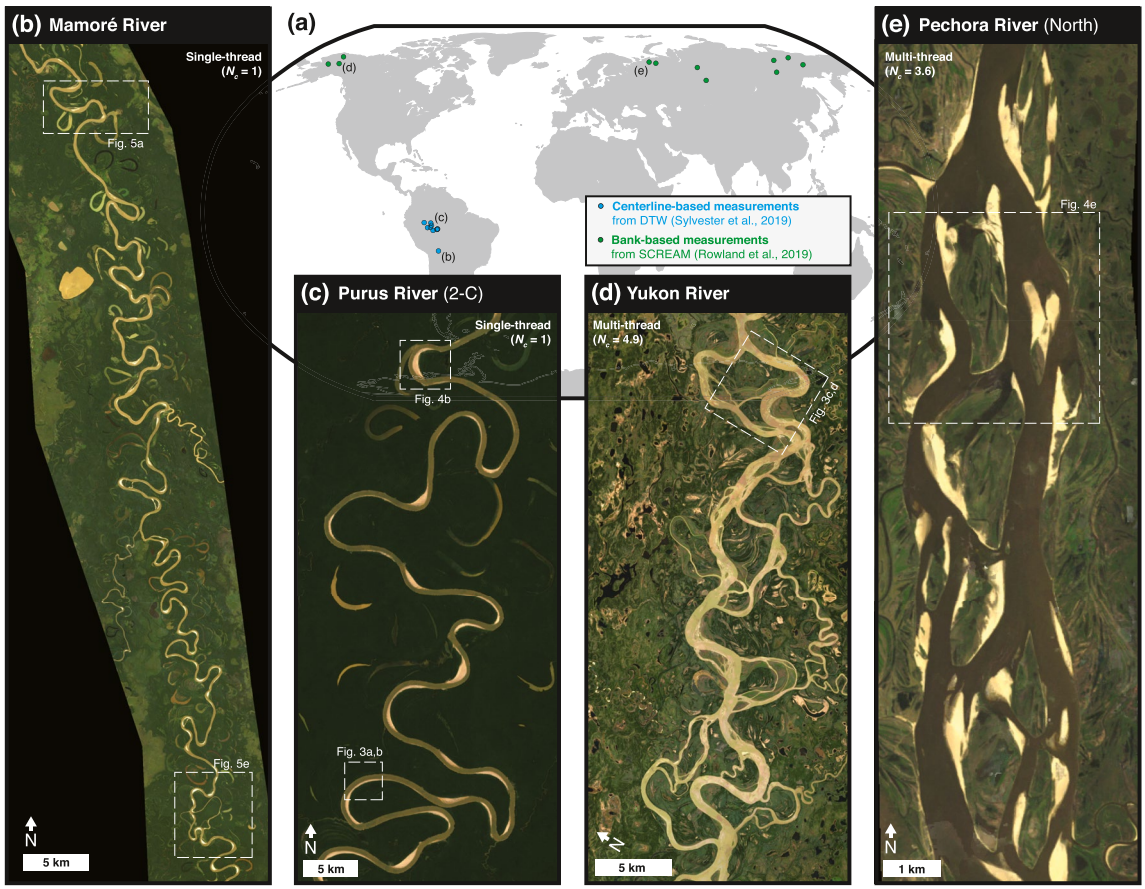

Figure 1. (a) World map showing the location of river reaches analyzed with particle image velocimetry, overlain with example NASA Landsat images of single-thread channels (b, c; $N_c = 1$, where N_c is the average number of sub-channels in a channel cross-section; Egozi & Ashmore, 2008) and multi-thread channels (d, e; $N_c > 1$). Previous work has quantified channel migration in these reaches using centerline-based dynamic time warping (blue circles; Sylvester et al., 2019) or bank-based Spatially Continuous Erosion and Accretion Measurements (green circles; Rowland et al., 2019). Dashed boxes denote areas shown in Figures 3–5.

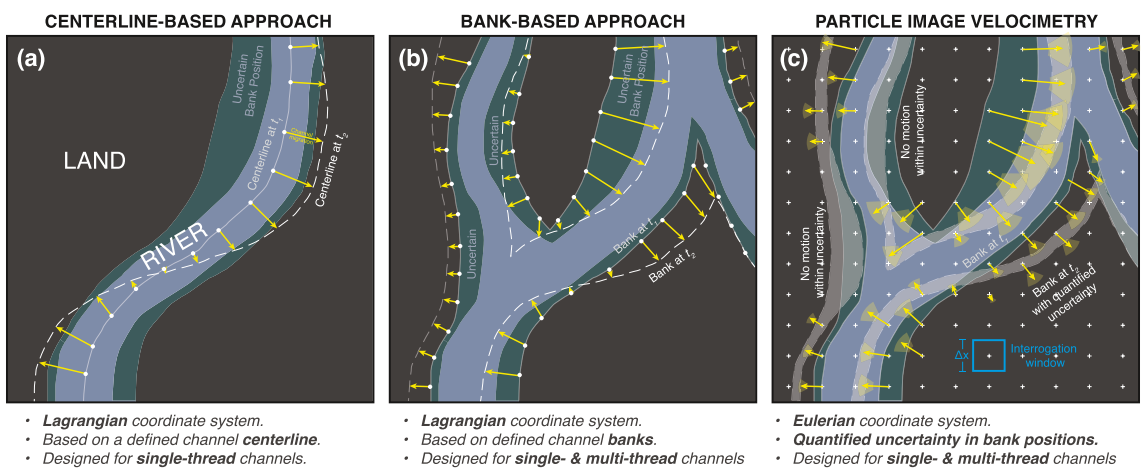

Figure 2. (a) Conceptual cartoon of a migrating river, showing how channel migration is quantified in a centerline-based approach. The river is defined in terms of its centerline at two times t_1 (gray solid line) and t_2 (white dashed line) and nearest-neighbor algorithms are used to determine the migration of the centerline (yellow). Panel (b) similar to panel (a) but here for a bank-based approach where the river is defined and tracked based on bank positions, which are sometimes uncertain (dark cyan regions). Panel (c) same as panel (b) but here for particle image velocimetry (PIV), where uncertainty in bank positions is quantified (gray shaded regions) and propagated into uncertainty in migration vectors (yellow shaded swaths). Blue square highlights an example PIV interrogation window, with input dimensions of Δx (Equation 1; Table 1).

Table 1
Summary of River Reaches Analyzed With Particle Image Velocimetry and Associated Input Parameters

River	Reach ID	Channel width, B (m)	Number of threads, N_c (–)	Estimated thread width, $b = B/N_c$ (m)	Estimated time to migrate one thread width, T_c (yr)	Optimum timestep, Δt (yr)	Interrogation window size, (m)		
							Pass 1 $4\Delta x$	Pass 2 $2\Delta x$	Pass 3 Δx
Mamoré	–	250	1	250	5	1	720	360	180
Yavarí	1-C	285	1	285	60	8	720	360	180
Juruá	1-A	287	1	287	30	4	720	360	180
Juruá	1-B	287	1	287	30	4	720	360	180
Juruá	2-A	287	1	287	20	3	720	360	180
Purus	1-A	304	1	304	30	4	720	360	180
Jutaí	1-B	313	1	313	60	8	720	360	180
Purus	2-A	416	1	416	30	4	960	480	240
Purus	2-B	416	1	416	30	4	960	480	240
Purus	2-C	460	1	460	30	4	960	480	240
Taz	–	366	1.1	332	30	4	720	360	180
Yana	–	494	1.1	446	40	5	960	480	240
Koyukuk	–	453	1.4	333	30	4	720	360	180
Indigirka	–	943	1.7	563	30	4	1,200	600	300
Pechora	South	1,744	2.2	806	15	2	1,680	840	420
Ob	–	1,463	2.6	557	30	4	1,200	600	300
Colville	–	1,079	2.8	382	10	1	960	480	240
Kolyma	–	1,425	3.2	442	10	1	960	480	240
Pechora	North	2,530	3.6	708	20	3	1,440	720	360
Lena	–	6,444	4.5	1,424	30	4	2,880	1,440	720
Yukon	–	2,041	4.9	420	30	4	960	480	240

Note. Reach ID numbers are those of Sylvester et al. (2019), with letters representing further sub-divisions for our analysis to maintain image dimensions of 50–150 channel-widths. Channel width (B) and number of threads (N_c) are reported in previous work (Rowland et al., 2019; Sylvester et al., 2019). Optimum timesteps (Δt) were calculated using Equation 2 and rounded to the nearest year. Pass-3 interrogation window sizes (Δx) were calculated using Equation 1 and rounded up to the nearest even number of Landsat pixels (equivalent to multiples of 60 m).

Here, we upscale the experimental PIV method to the global satellite archive. We integrate PIV analysis with established remote sensing methods for riverbank identification (Jones, 2015, 2019) and highlight compelling examples from NASA Landsat imagery. We compare PIV-derived results to published results from bank- and centerline-based approaches and demonstrate PIV's power to quantify spatiotemporal patterns in migration rate along single- and multi-thread river channels. Finally, we discuss the advantages and disadvantages of the PIV compared to other methods and the implications for leveraging PIV to interrogate global river response to climate change and human activities.

2. Materials and Methods

2.1. Upscaling PIV for Application to Rivers in the Global Satellite Archive

Our remote sensing approach for tracking riverbank migration with PIV builds upon the experimental framework developed by Chadwick, Steel, Williams-Schaetzel, et al. (2022). We briefly summarize their approach here and highlight the adaptations made for upscaling to global satellite data using 21 example river reaches selected based on the availability of published centerline- and bank-based migration measurements (Rowland et al., 2019; Sylvester et al., 2019). The reaches are located in South America and the Arctic, and span a wide range of migration speeds, avulsion and cutoff frequencies, and planform morphologies (as quantified by the reach-averaged

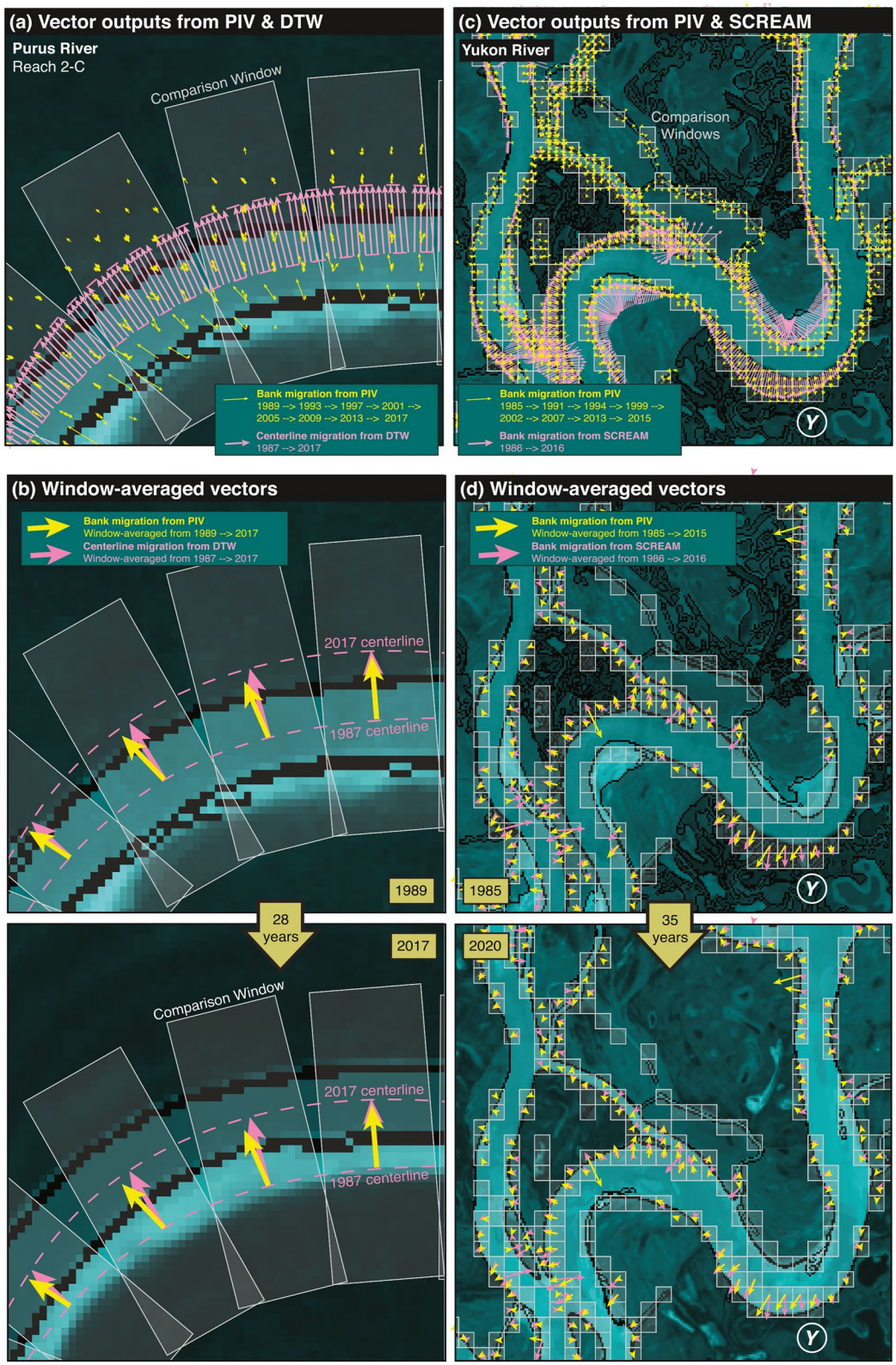

Figure 3.

number of channel threads, N_c; Table 1). Here, we chose to leverage remotely sensed imagery collected by the NASA Landsat mission because it offers a relatively high spatial resolution (30 m/pixel) over a long time interval (1985-present). However, the same PIV method can be applied to imagery from other sources such as ESA Sentinel-2 (Drusch et al., 2012; Marshall & Boshuizen, 2013). The method consists of three steps: image preparation, PIV implementation, and PIV postprocessing.

2.1.1. Image Preparation

The first step of the PIV method is *image preparation*, wherein Landsat images are downloaded and converted into binary masks of the channel for input to PIV (Chadwick, Steel, Williams-Schaetzel, et al., 2022). For upscaling to the satellite archive, this step was implemented using Google Earth Engine (Gorelick et al., 2017). We outlined a reach at each site (Figure 1; Table 1) that was approximately 50–150 channel-widths in length—large enough to capture several bends and bars while maintaining reasonable computational times for PIV (1–30 min per image pair). Within each outlined reach, we then downloaded NASA Landsat atmospherically corrected surface reflectance data from 1985 to 2021 with a resolution of 30 m/pixel (Landsat 5 TM, Landsat 7 ETM+ and Landsat 8 OLI/TIRS). Images were grouped by year and combined into median annual composites, which mitigated the effect of clouds and intra-annual river-stage variations (Langhorst & Pavelsky, 2023; Schwenk et al., 2017). The median surface-water extent in the annual composites may not be representative of the channel's surface-water extent during bankfull discharge, but we expect the median and bankfull extents to exhibit similar mobility unless the channel undergoes significant changes in cross-sectional geometry.

Composites were then binarized into water and non-water pixels using the USGS Dynamic Surface Water Extent (DSWE) procedure (Jones, 2015, 2019). The DSWE procedure employs a decision-tree structure based on several spectral indices, and is specifically designed for global Landsat applications and long-term consistency in performance. The procedure tests for the presence of surface water in each pixel at four confidence levels: high-confidence surface water, moderate-confidence water, conservative partial surface water, and aggressive partial surface water. We used results for each confidence level to threshold the color images, generating four distinct but defensible binary masks for a given annual composite image. We then filtered water pixels to exclude lakes, wetlands, and other unchannelized water bodies based on proximity and connectedness to global vector products of predicted channel location (Allen & Pavelsky, 2018; Yamazaki et al., 2019; Yang et al., 2020). Images were manually removed if they were blank or if they contained poor observation conditions (e.g., clouds or snow covering the vast majority of the image).

2.1.2. PIV Implementation

The second step is *PIV implementation*. Following previous work (Chadwick, Steel, Williams-Schaetzel, et al., 2022), we utilized the open-source MATLAB package PIVlab (Mathworks, 2021; Thielicke & Stamhuis, 2014). The PIV algorithm automatically evaluates the displacement of wetted channel areas between consecutive binary images through the cross-correlation of many nested sub-images, referred to as interrogation windows (Figure 2c). The primary user inputs for PIV are the size of these interrogation windows (Δx) and the timestep between consecutive images (Δt).

Following Chadwick, Steel, Williams-Schaetzel, et al. (2022), we set the dimensions of the final interrogation window for each river to be one half of the estimated thread width,

$$\Delta x = \frac{1}{2} b, \tag{1}$$

where Δx is the final window size (Pass 3) and $b = B/N_c$ is the estimated thread width based on the ratio of reported channel width B and thread count N_c (Table 1). This size is large enough to capture a distinct length of riverbank but not so large as to contain significant spatial gradients in velocity (Chadwick, Steel, Williams-Schaetzel, et al., 2022).

When entering the interrogation-window size into PIVlab, Δx was converted from units of meters into units of pixels using Landsat's image resolution (30 m/pixel) and rounded up to the nearest number of even pixels. This

Figure 3. (a) Example bend segment along the Purus River Reach 2-C, showing comparison between bank migration rates derived from particle image velocimetry (PIV; yellow arrows) and derived from dynamic time warping (DTW; magenta arrows). Light gray-shaded regions are comparison windows used for spatiotemporal averaging in (b). (b) Window-averaged migration vectors from 1989 (top) to 2017 (bottom). Background imagery is NASA Landsat grayscale recolored cyan for contrast, with black pixels along detected riverbanks (Jones, 2019). Panels (c, d) same as panels (a, b), but here for a segment of the Yukon River showing comparison between bank migration rates derived from PIV (yellow) and bank migration rates derived from Spatially Continuous Erosion and Accretion Measurements (SCREAM; magenta arrows) from 1985 to 2020. Bend labeled *Y* is discussed in the text (Section 3.2). Quantified uncertainty in PIV-vector directions and magnitudes is omitted here for visual clarity.

ensured that each image was assigned a consistent, evenly spaced grid of interrogation windows. To improve signal-to-noise ratios in the final correlation, we utilized larger preliminary interrogation windows set to fourfold and twofold Δx (Pass 1 and Pass 2 in Table 1) (Scarano & Riethmuller, 1999; Thielicke & Stamhuis, 2014; Westerweel, 1997). Following Equation 1, we expect random measurement error from PIV on the order of 5%–10% (Chadwick, Steel, Williams-Schaetzel, et al., 2022; Foucaut et al., 2004; Sciacchitano, 2019). Increasing Δx leads to an increase in random error. Decreasing Δx leads to a decrease in random error but also increases computer-processing times and can introduce systematic errors as Δx approaches the pixel size (Nogueira et al., 2001; Sciacchitano, 2019). To avoid these systematic errors, we focused our analysis on rivers with $\Delta x \geq 6$ pixels, corresponding to $b > 240$ m using Landsat's pixel size (30 m) and our rounding scheme (Table 1).

We selected a timestep between consecutive images that optimized PIV performance. Correlation signals are optimized when features move by roughly one quarter of the interrogation window size ($1/4\Delta x$) between images (Keane & Adrian, 1992). For measuring riverbank migration, this corresponds to riverbank migration distances of roughly one eighth the estimated thread width ($1/4\Delta x = 1/8b$; Equation 1). Following this guideline, we set the optimum image timestep as

$$\Delta t = \frac{1}{8} T_c, \tag{2}$$

where Δt is the optimum image timestep and T_c is the estimated time for a riverbank to migrate by one thread width. To evaluate Equation 2 for each reach, we estimated T_c based on visual inspection of the Landsat annual-composite color-image time series (Table 1). We started with the first Landsat image (from 1985) and compared it to each subsequent year in order. We visually identified the earliest subsequent image where at least one segment of one thread had clearly migrated a distance comparable to its own width since 1985. Then, we calculated the time difference between this image and the first image to estimate T_c. To promote the reproducibility of this inspection procedure, we rounded T_c to the nearest multiple of 5 years (Table 1). For two reaches (Yavarí 1-C and Jutaí 1-B), the fastest threads only migrated by about one-half of their width over the 36-year duration of imagery; in these cases, we estimated that it might take roughly 60 years for the threads to migrate by their own width ($T_c = 60$ years; Table 1).

Because we estimated T_c in Equation 2 based on relatively mobile banks along a study reach, PIV performance was optimized for these faster-migrating banks. Slower-migrating banks necessarily incurred higher random error—on the order of 5%–10% (Foucaut et al., 2004; Sciacchitano, 2019)—but this was negligible compared to uncertainty in the identified bank position (See Section 2.1.1). Importantly, the T_c-estimation procedure was designed to ensure that even the faster-migrating banks were unable to traverse an entire interrogation window within one timestep, thereby avoiding systematic errors in PIV that can arise when tracked features enter and exit their interrogation window (Nogueira et al., 2001; Sciacchitano, 2019). This approach of selecting Δt based on expected timescale of motion (Equation 2) is similar to more traditional applications of PIV measuring fluid dynamics (Keane & Adrian, 1992; Westerweel, 1997).

For uploading annual-composite images to PIVlab at the optimum timestep, we evaluated Equation 2 and rounded Δt to the nearest year (Table 1). For reaches with $\Delta t > 1$ yr, images were subsampled at intervals of the optimum timestep before being uploaded. For some image pairs, it was necessary to deviate slightly from the optimum image timestep due to data gaps in Landsat or poor observation conditions (e.g., clouds and snow; Section 2.1.1). For all analyzed reaches, we used PIVlab software version 2.31 with the FFT window deformation algorithm, the sub-pixel estimator (Gauss 2 × 3-point), and the Correlation Quality set to Extreme (Chadwick, Steel, Williams-Schaetzel, et al., 2022; Thielicke & Stamhuis, 2014).

To propagate uncertainty in channel positions to uncertainty in PIV measurements, we applied PIV separately to the four DSWE-thresholded binary-mask time series from the previous step (Section 2.1.1). Following previous work, we also tilted binary masks at four different angles relative to the PIV grid (0°, 15°, 30°, 45°) and applied PIV to each, in order to capture the additional uncertainty that stems from tracking features larger than the interrogation window (Chadwick, Steel, Williams-Schaetzel, et al., 2022). The result was 16 time series of PIV-derived vector fields (4 binary masks × 4 tilt angles) for a given image pair.

2.1.3. PIV Postprocessing

The third and final step is *PIV postprocessing* and remains unchanged when upscaled from experimental to remote-sensing methodologies. For each image pair, we used circular statistics to calculate the mean vector

field and the standard deviation in mean vector direction and magnitude (Chadwick, Steel, Williams-Schaetzel, et al., 2022; Curray, 1956; Miall, 1974). We filtered data to remove migration vectors where the standard deviation of vector magnitude exceeded the mean or the standard deviation of vector direction exceeded 180°. In addition, if PIV detected a vector in only one of the four binary masks, then the vector was deemed unreliable and discarded (Chadwick, Steel, Williams-Schaetzel, et al., 2022). Similar to experimental implementation, we found that filtering remotely sensed PIV data tended to remove roughly half the vectors in a field—usually in dry areas, channel interiors, and along ambiguous channel banks.

2.2. Comparing PIV to Centerline- and Bank-Based Approaches

We compared PIV-derived results for riverbank migration to previously published results from centerline- and bank-based methods. For centerline-based measurements, we leveraged data from meandering reaches in South America published by Sylvester et al. (2019). We focused our comparison on 10 reaches where the channel was wide enough for effective PIV analysis (>240 m wide, equivalent to >8 pixels in Landsat) (Nogueira et al., 2001; Sciacchitano, 2019) (Table 1). Sylvester et al. (2019) defined channel centerlines using a Python workflow that creates vector objects based on skeletonized water masks generated by the RivaMap semi-automated method (Isikdogan et al., 2017). Channel centerlines were then tracked between images using DTW (Lisiecki & Lisiecki, 2002; Sylvester et al., 2019). Data in areas where cutoffs and avulsions occurred were manually removed, which is common practice for centerline-based methods to avoid erroneous correlation of centerlines when the channel jumps course (Y. Li & Limaye, 2022; Schwenk et al., 2017; Sylvester et al., 2019).

Compared to centerline-based DTW measurements, PIV utilizes a different coordinate system (Figures 2a and 2c) and produced vector fields at higher temporal frequencies. For quantitative comparison, we spatiotemporally averaged the DTW and PIV vectors in evenly spaced comparison windows oriented along the channel centerline (Figure 3a). Because DTW tracks centerlines and PIV tracks banks (Figures 2a and 2c), it was necessary that each comparison window was wide enough to capture the centerline and both banks (Figure 3a). To achieve this, we set the cross-stream dimension to the DTW-derived displacement vector with a buffer of one channel-width on either side. The shorter, streamwise dimension of windows was set by the channel width (Table 1). Within each window, we spatiotemporally averaged vectors to generate mean PIV- and DTW-derived vectors that can be compared in terms of their migration rates (U_{PIV}, U_{DTW}) (Figure 3b). We calculated the discrepancy between window-averaged migration rates in terms of their normalized difference $\delta U = (U_{\mathrm{PIV}} - U_{\mathrm{DTW}})/U_{\mathrm{DTW}}$.

For bank-based measurements, we leveraged data from single- and multi-thread Arctic rivers collected by Rowland et al. (2019) (Table 1; Figure 1). Rowland et al. (2019) defined channel banks based on the presence of vegetation using GeniePro semi-automated workflow (Perkins et al., 2005), and calculated the linear rates of bank erosion and accretion using SCREAM (Rowland et al., 2016). We focused on 11 reaches spanning 50–150 channel-widths each, where the average channel-thread width was wide enough for PIV analysis (>240 m); and where banks were mobile enough to migrate by at least one-half the channel-thread width over the 36-year duration of Landsat imagery (i.e., the estimated migration timescale was ≤72 years; Table 1). We note that Rowland et al. (2019) record the SCREAM-derived erosion and accretion rates for each vector, but not the SCREAM-derived vector direction. In the absence of SCREAM-derived vector direction data, we approximated this data using the recorded bank aspect—defined as the direction perpendicular to the bankline pointing away from the channel (Rowland et al., 2016). The vector fields reproduced using the true migration rate and estimated migration direction were reasonable and consistent with water masks upon visual inspection (Figure 3c). However, we note this approximation should overestimate the amount of bank-perpendicular motion and underestimate the amount of bank-parallel motion compared to the true SCREAM vectors.

Bank-based SCREAM vectors are organized in a Lagrangian framework similar to centerline-based approaches, but in this case migration rates are calculated for each pixel along the detected bankline (Figure 2b). We implemented a similar window-averaging approach to compare SCREAM and PIV vectors (Figures 3c and 3d). Because both PIV and SCREAM are designed to track bank motions (Figures 2b and 2c), in this case we organized comparison windows in a rectilinear grid with window dimensions of one-half the average channel-thread width (Figures 3c and 3d). We computed the mean migration rates in each window (U_{PIV},U_{SCREAM}), as well as the migration-rate discrepancy $\delta U = (U_{\mathrm{PIV}} - U_{\mathrm{SCREAM}})/U_{\mathrm{SCREAM}}$.

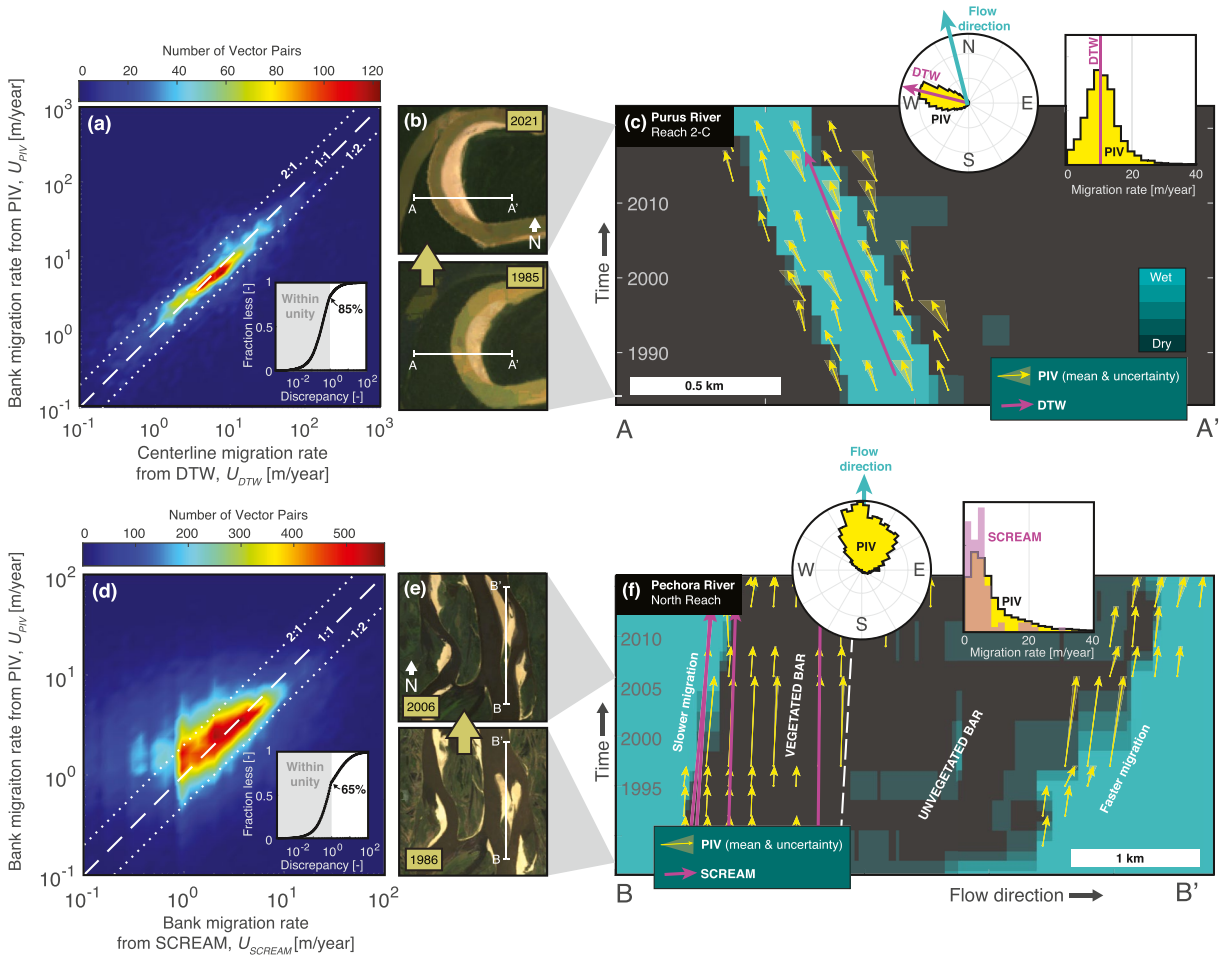

Figure 4. (a) Shaded density plot comparing migration rates derived from particle image velocimetry (U_{PIV}) to those derived from dynamic time warping (U_{DTW}) across all analyzed reaches (Figure 1a), spatiotemporally averaged within each comparison window (Figure 3a). White lines show trend for perfect agreement (dashed) and agreement within a factor of two (dotted). Inset shows cumulative frequency distribution of the fractional discrepancy in migration rate, defined as $(U_{PIV} - U_{DTW})/U_{DTW}$. (b) Example cross-section A–A' from a bend along Reach 2-C of the Purus River in 1985 and 2021. (c) Space-time diagram showing the evolution of the wetted channel along cross-section A–A' from 1985 to 2021, overlain with PIV-derived (yellow) and DTW-derived (magenta) migration vectors. Insets show histograms of migration direction and migration rate for A–A'. Panel (d) same as panel (a), but here for comparing PIV-derived migration rates to SCREAM-derived migration rates; discrepancy is defined as $(U_{PIV} - U_{SCREAM})/U_{SCREAM}$. Panels (e, f) same as panels (b, c), but here showing streamwise section B–B' along the Pechora River.

3. Results

3.1. Comparison Between PIV and Centerline-Based Measurements

We find remotely sensed channel migration vector fields derived from PIV are consistent with centerline-based measurements (Figure 4). The PIV-derived results for migration rate show close agreement with centerline-based DTW measurements across two orders of magnitude for all 10 sites (n = 16,835 vector pairs), with 85% of vector pairs consistent within unity ($\delta U < 1$) (Figure 4a). Similar agreement is found on a site-by-site basis (81%–91%; Figure S1 in Supporting Information S1). We expect some discrepancy between measured migration rates because PIV and DTW analyses use different algorithms for detecting channels (Isikdogan et al., 2017; Jones, 2015), and because available data spanned slightly different time intervals when computing window-based averages (e.g., Figure 3b).

The main difference between the two methods is that DTW measurements reflect the migration of the channel centerline whereas PIV tracks migration of the banks. Opposing banks and their centerline do not always migrate in sync, especially over shorter timescales (Eke, Czapiga, et al., 2014; Mason & Mohrig, 2019). For example, we consider a cross-section along a bend of the Purus River (Reach 2-C) (Figure 4b). Here, PIV and DTW show general agreement as the channel approximately migrated westward at ~10 m/year over the 36-year duration of

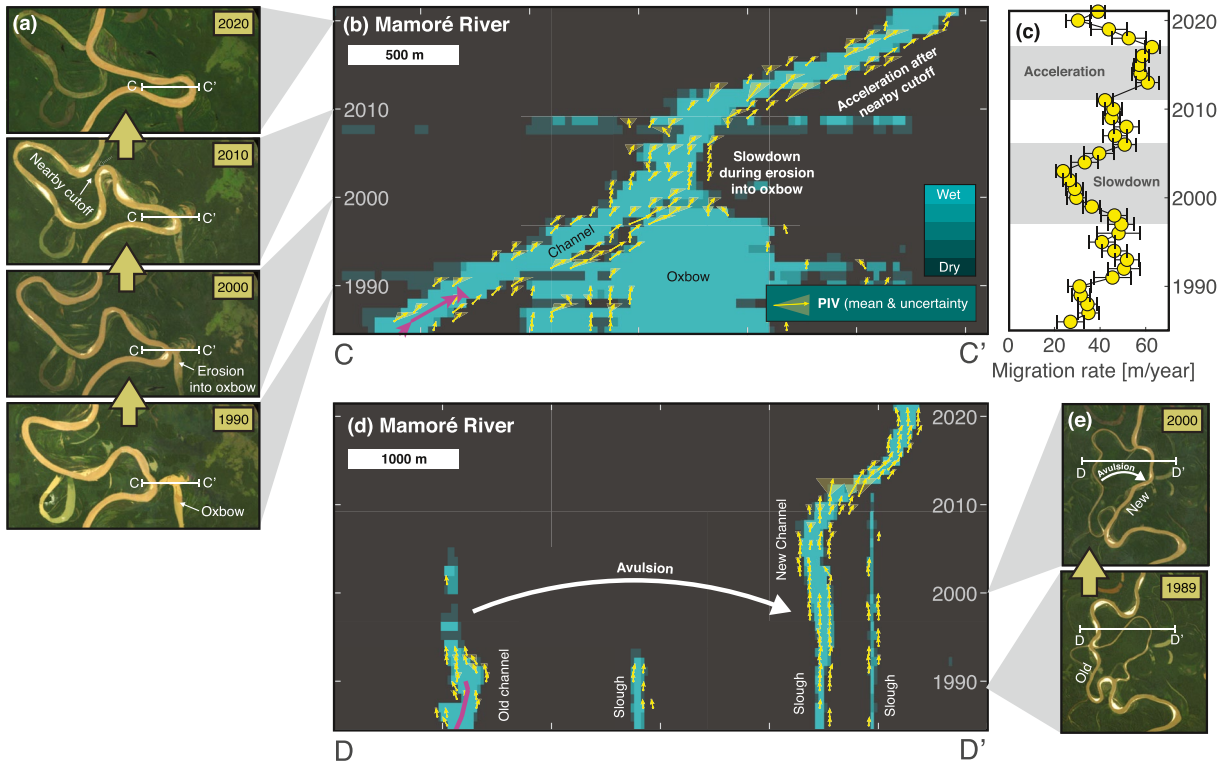

Figure 5. Advantages of using particle image velocimetry (PIV) to analyze riverbank migration, showcased along the Mamoré River. Panels (a, b) same as Figures 4b and 4c, but now for cross-section C–C'. Panel (c) Time series showing the 2-year mean and standard error of migration rates along C–C'. Shaded regions highlight periods when migration slowed as the channel eroded into an oxbow lake (1997–2006) and when migration accelerated after a nearby cutoff (2011–2016). Panels (d, e) same as panels (a, b), but now showing cross-section D–D'. Curved white arrow highlights channel avulsion, during which the old channel was abandoned in favor of a new channel, cannibalizing a former slough (1989–2000). PIV specifically targets bank migration and ignores displacement associated with avulsion.

Landsat (Figures 4b and 4c). Unlike DTW, PIV also characterizes the year-to-year variability in migration rate (9.7 ± 5.2 [3.2, 20.0] m/yr, where ± indicates one standard deviation from the mean and brackets denote 5th and 95th percentiles) and the variability in migration direction (83° ± 28° [39°, 135°], measured counter-clockwise from North) (Figure 4c inset). Although some of this variability can be attributed to propagated uncertainty from identified riverbank positions (Section 2.1), we expect that much of the signal reflects natural variability in migration dynamics. We find that differences in migration rates between opposing banks generally compensate for one another over timescales greater than about 5 years on the Purus River (Figure 4c), which is similar to field observations of the Trinity River (Mason & Mohrig, 2019). This balance between bank erosion and bar accretion rates maintains a relatively constant channel width (Figures 4b and 4c) that is characteristic of meandering rivers (Dunne & Jerolmack, 2020; Leopold & Maddock, 1953; Naito & Parker, 2019). We expect greater discrepancy would arise for channels undergoing significant widening or narrowing because associated bank adjustments are captured by PIV (Chadwick, Steel, Passalacqua, & Paola, 2022) but have relatively little impact on centerline positions (Eke, Czapiga, et al., 2014; Rowland et al., 2016).

3.2. Comparison Between PIV and Bank-Based Measurements

PIV-derived results for riverbank migration rate show agreement with bank-based SCREAM measurements over an order of magnitude for all 11 sites (n = 90,666 vector pairs), with 65% of vector pairs consistent within unity ($\delta U < 1$) (Figure 4d). This discrepancy is 20% greater than observed in the comparison to centerline-based methods (85% in Figure 4a) and ranges between 50% and 75% for a given site except for the Colville River (24%) (Figure S2 in Supporting Information S1). Part of this discrepancy can be attributed to the slightly different time intervals available for computing window-based averages (Figure 3d), and our approximation of SCREAM vector directions using the reported bank aspect (Rowland et al., 2016). Additional discrepancy arises from the fact that, unlike PIV, SCREAM does not feature a sub-pixel estimator. As a result, the east-west and north-south

components of SCREAM-derived displacement are assigned integer pixel values. This introduces a known systematic error in SCREAM (Rowland et al., 2016), which is apparent in our comparison by the grouping and relative paucity of SCREAM-derived migration rates less than ~1 m/y (Figure 4d): this corresponds to migration distances less than ~1 pixel (30 m) over the duration of available Landsat images (~30 yr).

The main difference between the two methods arises from how riverbanks are identified. For PIV, we identified banks based on the edge of surface water (DSWE confidence levels 1–4 in annual median composites), whereas for SCREAM, data banks were identified based on the edge of vegetation (Perkins et al., 2005; Rowland et al., 2019). Identifying channel banks based on the edge vegetation is common practice in studies of meandering rivers because the vegetation line generally migrates in sync with the channel and is insensitive to river stage (Constantine & Dunne, 2008; Dunne & Jerolmack, 2020; Eke, Parker, & Shimizu, 2014; Isikdogan et al., 2017). However, for multi-thread rivers, our results indicate that the migration rate of vegetation lines and surface-water edges is significantly decoupled. We highlight this point using an example bend of the Yukon River (Figures 3c and 3d, labeled *Y*). Along the outer eroding bank, the vegetation line was coincident with the water line, with PIV and SCREAM showing close agreement over 35 years (Figure 3d). On the inner bank, however, an unvegetated bar separated the vegetation line from water-line-confidence contours. Over 35 years, the vegetation line encroached ~500 m to fully vegetate the bar, whereas the water line remained stable within uncertainty. Differences between vegetated and unvegetated bank motions are most apparent in multi-thread channels with significant downstream bar migration. For example, we highlight a streamwise section along the Pechora River (North Reach; ~3 threads; Figure 4e). Section B–B' intersects a downstream-migrating mid-channel bar, where the upstream portion is vegetated and the downstream portion is unvegetated. Both PIV and SCREAM accurately track the motion of the vegetated bar, which migrated ~500 m northward over 36 years (~14 m/yr). However, only PIV tracks the unvegetated bar, which migrated about twice as fast (~30 m/yr). As a result, SCREAM data do not capture the highest rates in the PIV migration-rate distribution (~10–40 m/yr; Figure 4f inset). Similar discrepancies are found in other multi-thread sites, with site-by-site discrepancy (δU) positively correlated with the amount of downstream migration (Figure S3 in Supporting Information S1). The Colville features the most prominent unvegetated banks and mid-channel bars among the analyzed reaches, and consequently this reach exhibits the highest discrepancy between SCREAM and PIV (only 24% of vector pairs were consistent within unity; Figure S2 in Supporting Information S1).

3.3. River-Mobility Dynamics Captured by PIV

In this subsection, we highlight the dynamics of river mobility that can be extracted using PIV. As a motivating example, we present results from the most mobile reach analyzed in this study, along the Mamoré River, BO (Sylvester et al., 2019). PIV-derived vector fields show that this meandering channel migrated at 25.5 ± 27.2 [2.1, 77.3] m/yr and experienced multiple cutoff and avulsion events over the 36-year span of Landsat imagery (Figure 5). Along one bend C–C', the channel spent ~10 of these years migrating through a previously deposited oxbow lake (~1997–2006; Figures 5a and 5b; Movie S1). PIV-derived vector fields capture how the channel migrated more slowly while the oxbow lake was being eroded (Figures 5b and 5c), which may be linked to the cohesive oxbow-lake deposits resisting fluvial erosion, or to the hydraulic connection with the lake reducing the river's effective fluid-shear stress and erosion potential along the bank (Bogoni et al., 2017; Fisk, 1947; Hooke, 2004; Meakin et al., 1996; Sun et al., 1996). Five years later (in 2011), a nearby downstream bend experienced a neck cutoff (Figure 5a) and bend C–C' experienced a temporary increase in migration rate (Figure 5c). This acceleration may be linked to backwater effects or increased riverbed slope triggered by the cutoff—behavior that has been previously documented on the Ucayali River, PE (Schwenk & Foufoula-Georgiou, 2016).

Farther upstream along the Mamoré, an avulsion occurred in ~1995 (Figures 5d and 5e; Section D–D') (Movie S2). The avulsion rerouted flow from an old eastern channel to a new western channel, cannibalizing a small slough (Hajek & Edmonds, 2014; Kleinhans et al., 2013). PIV-derived vector fields along D–D' capture gradual migration of the old channel before the avulsion, and rapid migration of the new channel after avulsion (Figure 5d). The slough remained stationary, as illustrated by vertical vectors in the space-time diagram (Figure 5d). Importantly, PIV does *not* assign vectors to the displacement associated with the avulsion itself. This is because the PIV method is designed to track the translation of pre-existing channels through cross-correlation at the scale of the interrogation window (i.e., the scale of the channel width); PIV does not quantify the initiation or abandonment of channels (Chadwick, Steel, Williams-Schaetzel, et al., 2022).

4. Discussion

4.1. Advantages and Disadvantages of PIV for Remote Sensing of Riverbank Migration

Manual mapping of riverbank migration by trained geologists is infeasible given the sheer volume of the global satellite archive, leading to the development of automated methods based on tracking the channel's centerline (e.g., DTW; Figure 2a) (Lisiecki & Lisiecki, 2002; Sylvester et al., 2019) or the channel banks (e.g., SCREAM and REAL; Figure 2b) (Langhorst & Pavelsky, 2023; Rowland et al., 2016). Our results demonstrate that upscaled PIV (Figure 2c) presents a promising new alternative to other automated methods. PIV shows order-one consistency with centerline- and bank-based methods (Figures 4a and 4d) and offers three main advantages.

First, PIV is equally applicable to all planform morphologies—from single-thread channels (e.g., meandering rivers) to multi-thread channels (e.g., braided, anastomosing, and wandering rivers; Figure 1) (Eaton et al., 2010; Galeazzi et al., 2021; Latrubesse, 2008). This advantage stems from PIV's Eulerian coordinate system, which organizes vector fields in a grid that is independent of channel position or geometry (Figure 2c). Similarly broad applicability can be achieved using bank-based methods, but not centerline-based methods. Centerline-based methods are based in a Lagrangian coordinate system that organizes vectors along a designated channel centerline (Figure 2a), and so applicability is largely constrained to single-thread meandering channels where the main channel centerline can be well defined (Dey & Bhattacharya, 2014; Marra et al., 2014). PIV's broad applicability opens up avenues for future research comparing channel mobility across planform morphologies. For example, past work has investigated the hypotheses that migration rate scales with channel width (Hickin & Nanson, 1984), bend curvature (Y. Li & Limaye, 2022; Sylvester et al., 2019), cutoffs (Schwenk & Foufoula-Georgiou, 2016), bank strength (Ielpi et al., 2023), and sediment supply (Constantine et al., 2014) for single-thread meandering rivers. PIV offers means to further test these hypotheses and expand investigations to multi-thread channels. PIV can also be leveraged to explore planform-specific differences between riverbank erosion and bar accretion, which can help maintain the channel's width and potentially its planform morphology (Chadwick, Steel, Passalacqua, & Paola, 2022; Mason & Mohrig, 2019).

Second, PIV isolates channel mobility due to riverbank migration. This is because the PIV algorithm maps vectors based on the best-fit translation of existing channel areas from image to image (Chadwick, Steel, Williams-Schaetzel, et al., 2022; Keane & Adrian, 1992; Westerweel, 1997). The algorithm largely ignores mobility due to avulsions (Figures 5d and 5e; Movie S1) and cutoffs (Figures 5a and 5b; Movie S2) because these processes involve the initiation and abandonment of channel areas rather than translation (Chadwick, Steel, Williams-Schaetzel, et al., 2022). This contrasts with centerline- and bank-based methods, where reaches with avulsions and cutoffs generally need to be manually identified and removed prior to analysis (Sylvester et al., 2019); or procedurally identified and tracked differently than other reaches (Rowland et al., 2016). PIV's ability to isolate migration renders it well-suited for studying highly mobile rivers like the Mamoré where migration, avulsion, and cutoffs are all common (Figure 5). Disentangling total channel mobility into its constituent processes is valuable because channel migration and avulsion processes can pose distinct hazards requiring different management strategies to protect riverside communities (Mcewan et al., 2023; Moodie & Nittrouer, 2021; Thakur et al., 2012); and because migration and avulsion processes can respond differently to climate change and human activities (Bufe et al., 2019; Chadwick & Lamb, 2021; Jerolmack, 2009; Wickert et al., 2013).

Third, PIV allows for quantified uncertainty in riverbank positions to be directly propagated into uncertainty in migration. This is achieved by applying PIV to multiple confidence intervals of surface-water presence (DSWE) (Jones, 2015, 2019), and then calculating the standard deviation in the mean vector field using vector statistics (Figure 4c) (Chadwick, Steel, Williams-Schaetzel, et al., 2022). These vector statistics are made simple by PIV's Eulerian coordinate system because vectors are organized into a fixed grid where they can be directly compared across confidence intervals. In contrast, for centerline- and bank-based Lagrangian coordinate systems, the location and even the quantity of vectors will be different for each confidence interval, such that computing vector statistics across confidence intervals will be difficult or even impossible to implement. Identifying riverbanks is typically the greatest source of uncertainty in remote sensing studies of river channel mobility (Donovan et al., 2019; Lane et al., 2010; Nagel et al., 2022), so PIV's ability to propagate this uncertainty could prove invaluable for investigations of systematic differences between river systems (Langhorst & Pavelsky, 2023), as well as for investigations of global-scale temporal changes associated with climate change and human activities (Dethier et al., 2022). Quantified uncertainty will be vital as river-mobility research advances to investigate more

multi-thread river systems, where banks can be difficult to precisely constrain from remote sensing (Baki & Gan, 2012; Gupta et al., 2013).

PIV also comes with some disadvantages compared to existing methods. For example, centerline- and bank-based mobility methods can leverage their Lagrangian coordinate system to provide paired measurements of channel geometry and mobility (Rowland et al., 2016; Sylvester et al., 2019). However, due to its Eulerian coordinate system, the PIV algorithm makes no assumptions or calculations of channel geometry. Channel-geometry measurements must be made separately using other algorithms, such as RivGraph or rivMAP (Schwenk & Hariharan, 2021; Schwenk et al., 2017), or collected manually following established methods (Chadwick, Steel, Passalacqua, & Paola, 2022; Egozi & Ashmore, 2008). This additional step may pose an inconvenience for studies investigating the relationship between migration rates and geometric properties such as channel width and channel-bend curvature (Y. Li & Limaye, 2022; Sylvester et al., 2019). In the future, this disadvantage can be overcome by building computational suites that integrate PIV algorithms with existing geometry-focused algorithms.

Furthermore, extracting PIV vector fields can become computationally expensive for large data sets. For PIV analysis of Landsat data in this study, applying PIV to a single site required ~1–5 hr of computer-processing time on a high-performance computer—depending on the site's image size, the number of available images, and the PIV input parameters (Δx, Δt; Equations 1 and 2). Computer-processing time should increase when analyzing longer reaches than those in this study (>150 channel-widths), when leveraging data sets with higher image resolution (<30 m/pixel) and more available imagery than Landsat (>36 annual composites), and when thread width and mobility require smaller values of input Δx and Δt (Equations 1 and 2). Over large spatiotemporal scales, vector fields can become difficult to visualize (Figures 3a and 3c)—at least without vector averaging (Figures 3b and 3d) or timelapse videos (Movies S1 and S2). At some point, PIV analysis may be judged too computationally expensive, at least compared to relatively simple algorithms like those of centerline-based DTW (Lisiecki & Lisiecki, 2002; Sylvester et al., 2019). This disadvantage can be overcome by leveraging parallel-processing techniques available in PIVlab and MATLAB; by using high-performance-computing and visualization resources available at many universities and research facilities; and by future integration of PIV algorithms with powerful cloud computing planforms such as Google Earth Engine (Gorelick et al., 2017).

Even before overcoming PIV's disadvantages, we expect its benefits to outweigh the costs for many studies. For comparative studies of different river systems, PIV offers broad applicability across planform morphologies. For studying highly mobile rivers that move through a variety of processes, PIV offers a means to isolate and disentangle the component of motion associated with riverbank migration. And for investigations of river response to climate change and human activities, PIV offers a means to propagate uncertainties and establish baselines for significant response. On the other hand, for studies focused on the centerline migration, curvature, and width of single-thread meandering rivers, centerline-based methods may provide a more convenient and computationally expedient alternative to PIV.

4.2. The Importance of Selecting Riverbank Proxy: Waterline or Vegetation Line?

Remote-sensing studies of river mobility have typically identified bank positions based on either the edge of vegetation (Boruah et al., 2008; Donovan et al., 2019) or the edge of annual surface water (Lane et al., 2010; Langhorst & Pavelsky, 2023). Our comparative analysis shows that using the vegetation line as a proxy for the channel bank—a common work-around for single-thread rivers—is disadvantageous for multi-thread rivers because there is significant motion associated with unvegetated bars and banks that migrate out-of-sync with the vegetation line (Figures 3c, 4e, and 4f) (Constantine & Dunne, 2008; Dunne & Jerolmack, 2020; Eke, Parker, & Shimizu, 2014; Isikdogan et al., 2017). This disadvantage can be overcome by identifying channel positions based on water-surface presence (Jones, 2015, 2019; Sylvester et al., 2019), which enables waterlines to be tracked along both vegetated and unvegetated banks (Figures 4e and 4f). Unvegetated banks may migrate significantly faster than vegetated banks (Figure 4f), and can be distinguished from one another based on spectral indices (Kauth & Thomas, 1976; Valenza et al., 2022). Quantifying differences between vegetated and unvegetated banks may be crucial for unraveling the dynamics of different types of multi-thread channels, which are often classified based on whether mid-channel islands are unvegetated (in braided rivers) or vegetated (in anastomosing rivers) (Church & Rood, 1983; Eaton et al., 2010; Makaske, 2001). Furthermore, decoupling between water- and vegetation-lines may be especially pronounced for rivers experiencing climate-induced shrubification, as has been hypothesized for rivers in the Arctic (Ielpi et al., 2023).

Using water-surface presence as a proxy for bank position necessarily introduces uncertainty associated with variable river stages and wetted widths over the course of the annual hydrograph (Dong & Goudge, 2022; Limaye, 2017). Importantly, this drawback can be mitigated using annual-composite imagery, as we have done here. Annual composites recover the median spectral signature of water-surface presence for a given year and are thus relatively insensitive to seasonal variations in river stage (Langhorst & Pavelsky, 2023; Schwenk et al., 2017). The median surface-water extent may not be representative of bankfull surface-water extent, but we expect both to exhibit the same mobility unless the channel undergoes significant changes in cross-sectional geometry. As an alternative to annual composites, images can be compared using the wettest month in the year (Dong & Goudge, 2022) or using a reference water discharge where gage data permit (Limaye, 2017). Regardless of the image preparation, the uncertainty in wetted channel area can be quantified using confidence intervals and then propagated into PIV-derived mobility measurements (Figures 4c and 4f) (Chadwick, Steel, Williams-Schaetzel, et al., 2022).

4.3. Requirements for Applying PIV to Remotely Sensed Rivers Worldwide

Our results from 21 rivers worldwide demonstrate that PIV can accurately extract riverbank migration from remotely sensed imagery of channels with various sizes, shapes, and speeds. For successful PIV application to other rivers in future studies, we emphasize that river imagery should meet three main requirements. First, channel threads need to be large enough relative to the image resolution for coherent correlation of riverbanks between images. This is necessary to prevent systematic errors that arise when interrogation-window size approaches the pixel size (Nogueira et al., 2001; Sciacchitano, 2019). These errors are avoided when interrogation windows contain at least 10 pixels,

$$N_{\text{wind}} \gtrsim 10\,\text{pix}, \tag{3}$$

where $N_{\text{wind}} = \Delta x^2$ is the area of an interrogation window with dimensions Δx, expressed in terms of the number of constituent pixels. Plugging in our equation for window size (Equation 1) and rounding up to the nearest even number of pixels (Table 1), we find Equation 3 corresponds to a thread width b of at least eight pixels,

$$b \gtrsim 8\,\text{pix}. \tag{4}$$

Thus, channel threads should be at least eight pixels wide for the successful application of PIV from remotely sensed imagery. For the 30-m/pix resolution of Landsat, Equation 4 is satisfied by channel threads wider than 240 m (Table 1). Narrower rivers could be analyzed using higher-resolution imagery, such as ESA Sentinel-2 and PlanetScope (Drusch et al., 2012; Marshall & Boshuizen, 2013), so long as Equation 4 is satisfied at the corresponding image resolution. We emphasize that for application to multi-thread rivers, Equation 4 corresponds to the width of individual threads (b), not the total channel width (B). Thread width can be estimated by dividing the channel width by the number of threads ($b = B/N_c$; Table 1).

Second, successful PIV application requires that channel threads migrate fast enough to traverse a significant distance over the timespan of available imagery. This is necessary to ensure that river-mobility signals are significant compared to random error and uncertainty associated with PIV (Keane & Adrian, 1992). This requirement can be represented in terms of an upper limit of the thread migration timescale T_c,

$$F\,T_c \lesssim T_{\text{img}}, \tag{5}$$

where T_{img} is the timespan of available imagery, T_c is the estimated time it takes a thread to migrate its own width based on visual inspection (Table 1; Section 2.1.2), and F is the fraction of a thread width deemed significant. We recommend taking $F = 1/2$, meaning that at least some threads traverse at least one-half their width—equivalent to one PIV interrogation window (Equation 1)—over the timespan of available imagery. Based on visual inspection, we deemed this distance was significant enough such that we were confident that net movement of the waterlines across the timelapse of annual composite imagery reflected true riverbank migration, and not year-to-year changes in the hydrograph and wetted width. With $F = 1/2$ and the timespan of Landsat imagery used here ($T_{\text{img}} = 36$ years), Equation 5 indicates that successful PIV application requires estimated thread migration timescales of $T_c \lesssim 72$ years. Slower rivers (i.e., those with higher T_c) may be suitable for PIV in the future as Landsat missions continue to collect imagery and T_{img} increases. PIV analysis of more recent remote sensing data, like ESA Sentinel-2 and PlanetScope (Drusch et al., 2012; Marshall & Boshuizen, 2013), will necessarily be limited to faster rivers (i.e., those with lower T_c) due to their shorter timespan of available imagery T_{img}.

Finally, the third requirement is that channel threads migrate slowly enough to traverse less than one interrogation window between consecutive images. This is necessary to prevent systematic errors that arise when tracked features enter or exit a PIV interrogation window (Keane & Adrian, 1992; Nogueira et al., 2001; Sciacchitano, 2019). Because the interrogation-window size is selected to be one-half the thread width (Equation 1), this requirement can be expressed in terms of a lower limit on the estimated thread migration timescale T_c,

$$\frac{1}{2}T_c \gtrsim \Delta t_{img}, \tag{6}$$

where Δt_{img} is the time between consecutive images in the timelapse. With the Landsat annual composites used here, $\Delta t_{img} = 1$ year and so rivers with $T_c \gtrsim 2$ years satisfy Equation 6. For faster rivers (i.e., those with lower T_c), it should be possible to leverage monthly or even daily imagery where available to reduce Δt_{img} and satisfy Equation 6. However, we emphasize that doing so may introduce additional seasonal movement of waterlines between images due to the annual hydrograph and associated wetted-width variations. This additional signal could be mitigated by careful selection of imagery at a reference discharge (Limaye, 2017).

Together, these three requirements can be used to identify rivers that are wide enough (Equation 4), fast enough (Equation 5), and also slow enough (Equation 6) for PIV analysis using a given remote sensing data set.

4.4. Implications for Interrogating River Response to Climate Change and Human Activities

Our results demonstrate how PIV offers a means to efficiently extract river migration data (Figures 4 and 5) that can inform scientists, engineers, and policymakers as to how rivers are responding to our rapidly changing world. For example, previous work has identified systematic shifts in water and sediment supply associated with climate warming, damming, and deforestation (Dethier et al., 2022; D. Li et al., 2021; T. Li et al., 2020), as well as changes in bank-strength due to Arctic shrubification (Ielpi et al., 2023), all of which could be driving river-mobility changes detectable with PIV. PIV is also readily applicable to multi-thread distributary channels (Figure 2c), where migration may be influenced by sea-level rise and other coastal processes (Lentsch et al., 2018; Wickert et al., 2013; Wilson & Goodbred, 2015).

Importantly, cutoffs and avulsions are largely ignored by the PIV algorithm (Figure 5d; Movies S1 and S2), consistent with earlier experimental applications (Chadwick, Steel, Williams-Schaetzel, et al., 2022). This aspect of PIV could prove invaluable for interrogating river response because channel migration may respond differently compared to channel avulsion in the face of environmental change (Bentley Sr et al., 2016; Blum & Törnqvist, 2000; Nanson & Hickin, 1986). For example, laboratory experiments suggest that migration rate is reduced during sea-level rise (Bufe et al., 2019; Chadwick, Steel, Williams-Schaetzel, et al., 2022) whereas the frequency of river avulsion increases (Chadwick, Steele, Silvestre, & Lamb, 2022; Jerolmack, 2009; Martin et al., 2009). PIV provides valuable means to test such hypotheses on natural systems in the global satellite archive, by strategically isolating the component of river mobility associated with riverbank migration (Figure 5d; Movies S1 and S2) (Chadwick, Steel, Williams-Schaetzel, et al., 2022).

To identify significant signals of river response to climate change and human activities, it is necessary to also characterize the baseline of natural variability (Jerolmack & Paola, 2010; Wohl et al., 2005). The rich vector fields derived from PIV analysis are well-suited for characterizing natural variability in migration rate, including spatial differences in migration rate linked to vegetation (Figure 4f) (Peixoto et al., 2009; Tal et al., 2013); temporary slowdowns in migration rate associated with oxbow-lake connection and erosion (Figures 5b and 5c) (Bogoni et al., 2017; Fisk, 1947; Hooke, 2004; Meakin et al., 1996; Sun et al., 1996); as well as temporary accelerations in migration rate triggered by nearby cutoffs (Figure 5a) (Schwenk & Foufoula-Georgiou, 2016). Furthermore, the quantified uncertainty in local measurements captured by PIV represents a major step forward for global-scale analysis (Langhorst & Pavelsky, 2023). Quantified uncertainty and baselines of variability will allow researchers to rigorously evaluate hypotheses and models of river response to climate change that remain largely untested on modern natural systems (Chadwick & Lamb, 2021; Hariharan et al., 2022; Limaye, 2020; Wickert et al., 2013). Validating such models with PIV-derived measurements will help improve predictions for future erosion hazards in the face of climate change, and help inform sustainable management of watersheds subject to damming and deforestation (Church & Ferguson, 2015; Dethier et al., 2022; Passalacqua et al., 2021).

5. Conclusions

We upscaled PIV techniques from laboratory flume studies to global remote sensing of riverbank migration (Figure 1). We find that:

1. PIV can be applied to satellite imagery like NASA Landsat to automatically and efficiently quantify local rates and directions of gradual riverbank migration, and by design exclude abrupt channel-jumping events such as cutoffs and avulsions (Figure 5).
2. PIV-derived results are consistent with published results from centerline-based approaches (Figures 2a and 4a–4c) and bank-based approaches (Figures 2b and 4d–4f), with average migration rates showing agreement within unity ($\delta U < 1$) for 85% and 65% of data respectively. Discrepancies are primarily attributed to differences in what features are being tracked (centerlines vs. banks) and differences in how banks are identified (e.g., based on the edge of surface water or the edge of vegetation) (Figure 4).
3. Unlike centerline-based methods, PIV is equally applicable to single- and multi-thread river channels (Figure 1; Table 1) and is able to track the independent motions of opposing riverbanks, which may be temporally out-of-phase (Figure 4c) (Eke, Czapiga, et al., 2014; Mason & Mohrig, 2019).
4. Unlike bank-based methods, PIV is based on an Eulerian (i.e., grid-based) coordinate system (Figure 2) that facilitates the propagation of uncertainty associated with ambiguous riverbank positions. This is especially important for multi-thread rivers, where significant differences in mobility may be detected depending on whether the riverbank is identified based on the edge of surface water or the edge of vegetation (Figure 4f).
5. The PIV method provides a means to accurately, efficiently, and reproducibly extract the wealth of migration data in the global satellite archive, opening up new opportunities to investigate and test hypotheses about how rivers are responding to climate change and human activities (Chadwick & Lamb, 2021; Hariharan et al., 2022; Limaye, 2020; Wickert et al., 2013).

Data Availability Statement

The data and codes underlying this study are publicly available on the Dryad repository (https://doi.org/10.25349/D9HG82) and Zenodo (https://doi.org/10.5281/zenodo.7747389). Data were analyzed using Google Earth Engine available at earthengine.google.com (Gorelick et al., 2017) and MATLAB R2021b software available at www.mathworks.com (MATLAB, Mathworks, 2021). Step-by-step instructions and example code showing how to apply the PIV method are publicly available in the SEAD repository (http://doi.org/10.26009/s0ECKYD5).

Acknowledgments
This research was supported by the NSF Grants EAR 1935669 and EAR 2310740 to Ganti. The authors thank Jessica Fayne and students of the UC Santa Barbara's GEOG288VG class of Fall 2022 for insightful discussions.

References

Allen, G. H., & Pavelsky, T. M. (2018). Global extent of rivers and streams. *Science*, *361*(6402), 585–588. https://doi.org/10.1126/science.aat0636

Baki, A. B. M., & Gan, T. Y. (2012). Riverbank migration and island dynamics of the braided Jamuna River of the Ganges—Brahmaputra basin using multi-temporal Landsat images. *Quaternary International*, *263*, 148–161. https://doi.org/10.1016/j.quaint.2012.03.016

Bentley, S. J., Blum, M. D., Maloney, J., Pond, L., & Paulsell, R. (2016). The Mississippi River source-to-sink system: Perspectives on tectonic, climatic, and anthropogenic influences, Miocene to Anthropocene. *Earth-Science Reviews*, *153*, 139–174. https://doi.org/10.1016/j.earscirev.2015.11.001

Best, J. (2019). Anthropogenic stresses on the world's big rivers. *Nature Geoscience*, *12*(1), 7–21. https://doi.org/10.1038/s41561-018-0262-x

Blum, M. D., & Törnqvist, T. E. (2000). Fluvial responses to climate and sea-level change: A review and look forward. *Sedimentology*, *47*(SUPPL. 1), 2–48. https://doi.org/10.1046/j.1365-3091.2000.00008.x

Bogoni, M., Putti, M., & Lanzoni, S. (2017). Modeling meander morphodynamics over self-formed heterogeneous floodplains. *Water Resources Research*, *53*(6), 5137–5157. https://doi.org/10.1002/2017WR020726

Boruah, S., Gilvear, D. J., Hunter, P., & Sharma, N. (2008). Quantifying channel planform and physical habitat dynamics on a large braided river using satellite data—The Brahmaputra, India. *River Research and Applications*, *24*(5), 650–660. https://doi.org/10.1002/rra.1132

Brooke, S., Chadwick, A. J., Silvestre, J., Lamb, M. P., Edmonds, D. A., & Ganti, V. (2022). Where rivers jump course. *Science*, *376*(6596), 987–990. https://doi.org/10.1126/science.abm1215

Bufe, A., Turowski, J. M., Burbank, D. W., Paola, C., Wickert, A. D., & Tofelde, S. (2019). Controls on the lateral channel-migration rate of braided channel systems in coarse non-cohesive sediment. *Earth Surface Processes and Landforms*, *44*(14), 2836. https://doi.org/10.1002/esp.4710

Chadwick, A. J., & Lamb, M. P. (2021). Climate-change controls on river delta avulsion location and frequency. *Journal of Geophysical Research: Earth Surface*, *126*(6), e2020JF005950. https://doi.org/10.1029/2020jf005950

Chadwick, A. J., Steel, E., Passalacqua, P., & Paola, C. (2022). Differential bank migration limits the lifespan and width of braided channel threads. *Water Resources Research*, *58*(8), e2021WR031236. https://doi.org/10.1029/2021WR031236

Chadwick, A. J., Steel, E., Williams-Schaetzel, R. A., Passalacqua, P., & Paola, C. (2022). Channel migration in experimental river networks mapped by particle image velocimetry. *Journal of Geophysical Research: Earth Surface*, *127*(1), e2021JF006300. https://doi.org/10.1029/2021jf006300

Chadwick, A. J., Steele, S., Silvestre, J., & Lamb, M. P. (2022). Effect of sea-level change on river avulsions and stratigraphy for an experimental lowland delta. *Journal of Geophysical Research: Earth Surface*, *127*(7), e2021JF006422. https://doi.org/10.1029/2021jf006422

Chamberlin, E. P., & Hajek, E. A. (2019). Using bar preservation to constrain reworking in channel-dominated fluvial stratigraphy. *Geology*, *47*(6), 531–534. https://doi.org/10.1130/G46046.1

Church, M., & Ferguson, R. I. (2015). Morphodynamics: Rivers beyond steady state. *Water Resources Research*, *51*(4), 1883–1897. https://doi.org/10.1002/2014WR016862

Church, M., & Rood, R. (1983). Catalogue of alluvial river channel regime data.

Constantine, J. A., & Dunne, T. (2008). Meander cutoff and the controls on the production of oxbow lakes. *Geology*, *36*(1), 23–26. https://doi.org/10.1130/G24130A.1

Constantine, J. A., Dunne, T., Ahmed, J., Legleiter, C., & Lazarus, E. D. (2014). Sediment supply as a driver of river meandering and floodplain evolution in the Amazon Basin. *Nature Geoscience*, *7*(12), 899–903. https://doi.org/10.1038/ngeo2282

Curray, J. R. (1956). The analysis of two-dimensional orientation data. *Geology*, *64*(2), 117–131. https://doi.org/10.1086/626329

Dethier, E. N., Renshaw, C. E., & Magilligan, F. J. (2022). Rapid changes to global river suspended sediment flux by humans. *Science*, *376*(6600), 1447–1452. https://doi.org/10.1126/science.abn7980

Dey, A., & Bhattacharya, R. K. (2014). Monitoring of river center line and width—A study on river Brahmaputra. *Journal of the Indian Society of Remote Sensing*, *42*(2), 475–482. https://doi.org/10.1007/s12524-013-0277-0

Dillabaugh, C. R., Niemann, K. O., & Richardson, D. E. (2002). Semi-automated extraction of rivers from digital imagery. *GeoInformatica*, *6*(3), 263–284. https://doi.org/10.1023/a:1019718019825

Dong, T. Y., & Goudge, T. A. (2022). Quantitative relationships between river and channel-belt planform patterns. *Geology*, *50*(9), 1–5. https://doi.org/10.1130/g49935.1

Donovan, M., Belmont, P., Notebaert, B., Coombs, T., Larson, P., & Souffront, M. (2019). Accounting for uncertainty in remotely-sensed measurements of river planform change. *Earth-Science Reviews*, *193*, 220–236. https://doi.org/10.1016/j.earscirev.2019.04.009

Douglas, M. M., Li, G. K., Fischer, W. W., Rowland, J. C., Kemeny, P. C., West, A. J., et al. (2021). Organic carbon burial by river meandering partially offsets bank-erosion carbon fluxes in a discontinuous permafrost floodplain. *Earth Surface Dynamics*, *10*(3), 421–435.

Drusch, M., del Bello, U., Carlier, S., Colin, O., Fernandez, V., Gascon, F., et al. (2012). Sentinel-2: ESA's optical high-resolution mission for GMES operational services. *Remote Sensing of Environment*, *120*, 25–36. https://doi.org/10.1016/j.rse.2011.11.026

Dunne, K. B. J., & Jerolmack, D. J. (2020). What sets river width? *Science Advances*, *6*(41), 1–9. https://doi.org/10.1126/sciadv.abc1505

Eaton, B. C., Millar, R. G., & Davidson, S. (2010). Channel patterns: Braided, anabranching, and single-thread. *Geomorphology*, *120*(3–4), 353–364. https://doi.org/10.1016/j.geomorph.2010.04.010

Egozi, R., & Ashmore, P. (2008). Defining and measuring braiding intensity. *Earth Surface Processes and Landforms*, *34*(March), 613–628. https://doi.org/10.1002/esp

Einstein, A. (1926). The cause of the formation of meanders in the courses of rivers and of the so-called Baer's law. *Naturwissenschaften*, *14*(11), 223–224. https://doi.org/10.1007/bf01510300

Eke, E., Czapiga, M. J., Viparelli, E., Shimizu, Y., Imran, J., Sun, T., & Parker, G. (2014). Coevolution of width and sinuosity in meandering rivers. *Journal of Fluid Mechanics*, *760*(September 2015), 127–174. https://doi.org/10.1017/jfm.2014.556

Eke, E., Parker, G., & Shimizu, Y. (2014). Numerical modeling of erosional and depositional bank processes in migrating river bends with self-formed width: Morphodynamics of bar push and bank pull. *Journal of Geophysical Research: Earth Surface*, *119*(2), 1455–1483. https://doi.org/10.1002/2013JF003020.Received

Fisk, H. N. (1947). *Fine-grained alluvial deposits and their effects on Mississippi River activity*. Mississippi River Commission.

Foucaut, J. M., Miliat, B., Perenne, N., & Stanislas, M. (2004). Characterization of different PIV algorithms using the EUROPIV synthetic image generator and real images from a turbulent boundary layer. In *Particle image velocimetry: Recent improvements* (pp. 163–185). Springer.

Galeazzi, C. P., Almeida, R. P., & do Prado, A. H. (2021). Linking rivers to the rock record: Channel patterns and paleocurrent circular variance. *Geology*, *49*(11), 1402–1407. https://doi.org/10.1130/G49121.1

Ganti, V., Hajek, E. A., Leary, K., Straub, K. M., & Paola, C. (2020). Morphodynamic hierarchy and the fabric of the sedimentary record. *Geophysical Research Letters*, *47*(14), e2020GL087921. https://doi.org/10.1029/2020GL087921

Giosan, L., Clift, P. D., Macklin, M. G., Fuller, D. Q., Constantinescu, S., Durcan, J. A., et al. (2012). Fluvial landscapes of the Harappan civilization. *Proceedings of the National Academy of Sciences*, *109*(26), E1688–E1694. https://doi.org/10.1073/pnas.1112743109/-/DCSupplemental

Gleick, P. H. (2003). Global freshwater resources: Soft-path solutions for the 21st century. *Science*, *302*(5650), 1524–1528. https://doi.org/10.1126/science.1089967

Gorelick, N., Hancher, M., Dixon, M., Ilyushchenko, S., Thau, D., & Moore, R. (2017). Google Earth Engine: Planetary-scale geospatial analysis for everyone. *Remote Sensing of Environment*, *202*, 18–27. https://doi.org/10.1016/j.rse.2017.06.031

Gupta, N., Atkinson, P. M., & Carling, P. A. (2013). Decadal length changes in the fluvial planform of the river Ganga: Bringing a mega-river to life with Landsat archives. *Remote Sensing Letters*, *4*(1), 1–9. https://doi.org/10.1080/2150704x.2012.682658

Hajek, E. A., & Edmonds, D. A. (2014). Is river avulsion style controlled by floodplain morphodynamics? *Geology*, *42*(3), 199–202. https://doi.org/10.1130/G35045.1

Hariharan, J., Passalacqua, P., Xu, Z., Michael, H. A., Steel, E., Chadwick, A., et al. (2022). Modeling the dynamic response of river deltas to sea-level rise acceleration. *Journal of Geophysical Research: Earth Surface*, *127*(9), e2022JF006762. https://doi.org/10.1029/2022JF006762

Hickin, E. J., & Nanson, G. C. (1984). Lateral migration rates of river bends. *Journal of Hydraulic Engineering*, *110*(11), 1557–1567. https://doi.org/10.1061/(ASCE)0733-9429(1987)113:7(915)

Hooke, J. M. (2004). Cutoffs galore!: Occurrence and causes of multiple cutoffs on a meandering river. *Geomorphology*, *61*(3–4), 225–238. https://doi.org/10.1016/j.geomorph.2003.12.006

Ielpi, A., Lapôtre, M. G. A., Finotello, A., & Roy-Léveillée, P. (2023). Large sinuous rivers are slowing down in a warming Arctic. *Nature Climate Change*, *13*(4), 375–381. https://doi.org/10.1038/s41558-023-01620-9

Isikdogan, F., Bovik, A., & Passalacqua, P. (2017). RivaMap: An automated river analysis and mapping engine. *Remote Sensing of Environment*, *202*, 88–97. https://doi.org/10.1016/j.rse.2017.03.044

Jerolmack, D. J. (2009). Conceptual framework for assessing the response of delta channel networks to Holocene sea level rise. *Quaternary Science Reviews*, *28*(17–18), 1786–1800. https://doi.org/10.1016/j.quascirev.2009.02.015

Jerolmack, D. J., & Paola, C. (2010). Shredding of environmental signals by sediment transport. *Geophysical Research Letters*, *37*(19), L19401. https://doi.org/10.1029/2010gl044638

Jones, J. (2015). Efficient wetland surface water detection and monitoring via landsat: Comparison with in situ data from the everglades depth estimation network. *Remote Sensing*, *7*(9), 12503–12538. https://doi.org/10.3390/rs70912503

Jones, J. (2019). Improved automated detection of subpixel-scale inundation-revised Dynamic Surface Water Extent (DSWE) partial surface water tests. *Remote Sensing*, *11*(4), 374. https://doi.org/10.3390/rs11040374

Kauth, R. J., & Thomas, G. S. (1976). The tasselled cap: A graphic description of the spectral-temporal development of agricultural crops as seen by LANDSAT. Retrieved from http://docs.lib.purdue.edu/lars_symphttp://docs.lib.purdue.edu/lars_symp/159

Keane, R. D., & Adrian, R. J. (1992). Theory of cross-correlation analysis of PIV images. *Applied Scientific Research*, *49*(3), 191–215. https://doi.org/10.1007/bf00384623

Kidder, T. R., & Liu, H. (2017). Bridging theoretical gaps in geoarchaeology: Archaeology, geoarchaeology, and history in the yellow river valley, China. *Archaeological and Anthropological Sciences*, *9*(8), 1585–1602. https://doi.org/10.1007/s12520-014-0184-5

Kleinhans, M. G., Ferguson, R. I., Lane, S. N., & Hardy, R. J. (2013). Splitting rivers at their seams: Bifurcations and avulsion. *Earth Surface Processes and Landforms*, *38*(1), 47–61. https://doi.org/10.1002/esp.3268

Lane, S. N., Widdison, P. E., Thomas, R. E., Ashworth, P. J., Best, J. L., Lunt, I. A., et al. (2010). Quantification of braided river channel change using archival digital image analysis. *Earth Surface Processes and Landforms*, *35*(8), 971–985. https://doi.org/10.1002/esp.2015

Langhorst, T., & Pavelsky, T. (2023). Global observations of riverbank erosion and accretion from landsat imagery. *Journal of Geophysical Research: Earth Surface*, *128*(2), e2022JF006774. https://doi.org/10.1029/2022JF006774

Latrubesse, E. M. (2008). Patterns of anabranching channels: The ultimate end-member adjustment of mega rivers. *Geomorphology*, *101*(1–2), 130–145. https://doi.org/10.1016/j.geomorph.2008.05.035

Lentsch, N., Finotello, A., & Paola, C. (2018). Reduction of deltaic channel mobility by tidal action under rising relative sea level. *Geology*, *46*(7), 599–602. https://doi.org/10.1130/g45087.1

Leopold, L. B., & Maddock, T. (1953). *The hydraulic geometry of stream channels and some physiographic implications* (Vol. 252). US Government Printing Office. https://doi.org/10.3133/pp252

Li, D., Lu, X., Overeem, I., Walling, D. E., Syvitski, J., Kettner, A. J., et al. (2021). Exceptional increases in fluvial sediment fluxes in a warmer and wetter High Mountain Asia. *Science*, *374*(6567), 599–603. https://doi.org/10.1126/science.abi9649

Li, T., Wang, S., Liu, Y., Fu, B., & Gao, D. (2020). Reversal of the sediment load increase in the Amazon basin influenced by divergent trends of sediment transport from the Solimões and Madeira Rivers. *Catena*, *195*, 104804. https://doi.org/10.1016/j.catena.2020.104804

Li, Y., & Limaye, A. B. (2022). Testing predictions for migration of meandering rivers: Fit for a curvature-based model depends on streamwise location and timescale. *Journal of Geophysical Research: Earth Surface*, *127*(12), e2022JF006776. https://doi.org/10.1029/2022JF006776

Limaye, A. B. (2020). How do braided rivers grow channel belts? *Journal of Geophysical Research: Earth Surface*, *125*(8), e2020JF005570. https://doi.org/10.1029/2020JF005570

Limaye, A. B. (2017). Extraction of multithread channel networks with a reduced-complexity flow model. *Journal of Geophysical Research: Earth Surface*, *122*(10), 1972–1990. https://doi.org/10.1002/2016JF004175

Lisiecki, L. E., & Lisiecki, P. A. (2002). Application of dynamic programming to the correlation of paleoclimate records. *Paleoceanography*, *17*(4), 1-1–1-12. https://doi.org/10.1029/2001pa000733

Loveland, T. R., & Dwyer, J. L. (2012). Landsat: Building a strong future. *Remote Sensing of Environment*, *122*(October 2000), 22–29. https://doi.org/10.1016/j.rse.2011.09.022

Lynds, R. M., & Hajek, E. A. (2006). Conceptual model for predicting mudstone dimensions in sandy braided-river reservoirs. *American Association of Petroleum Geologists Bulletin*, *90*(8), 1273–1288. https://doi.org/10.1306/03080605051

Makaske, B. (2001). Anastomosing rivers: A review of their classification, origin and sedimentary products. *Earth-Science Reviews*, *53*(3–4), 149–196. https://doi.org/10.1016/s0012-8252(00)00038-6

Marra, W. A., Kleinhans, M. G., & Addink, E. A. (2014). Network concepts to describe channel importance and change in multichannel systems: Test results for the Jamuna River, Bangladesh. *Earth Surface Processes and Landforms*, *39*(6), 766–778. https://doi.org/10.1002/esp.3482

Marshall, W., & Boshuizen, C. (2013). Planet labs' remote sensing satellite system. In *Proceedings of the small satellite conference, pre-conference: CubeSat developers' workshop* (p. 7). Retrieved from https://www.planet.com/

Martin, J., Sheets, B., Paola, C., & Hoyal, D. (2009). Influence of steady base-level rise on channel mobility, shoreline migration, and scaling properties of a cohesive experimental delta. *Journal of Geophysical Research*, *114*(F3), F03017. https://doi.org/10.1029/2008JF001142

Mason, J., & Mohrig, D. (2019). Differential bank migration and the maintenance of channel width in meandering river bends. *Geology*, *47*(12), 1136–1140. https://doi.org/10.1130/G46651.1

Mathworks. (2021). MATLAB 9.11.0.1769968 (R2021b) [Software]. Matlab. Retrieved from https://www.mathworks.com/products/matlab.html

Mcewan, E., Stahl, T., Howell, A., Langridge, R., & Wilson, M. (2023). Coseismic river avulsion on surface rupturing faults: Assessing earthquake-induced flood hazard. *Science Advances*, *9*(18), eadd2932. https://doi.org/10.1126/sciadv.add2932

Meakin, P., Sun, T., Jossang, T., & Schwarz, K. (1996). A simulation model for meandering rivers and their associated sedimentary environments. *Physica A*, *233*(3–4), 606–618. https://doi.org/10.1016/s0378-4371(96)00197-5

Miall, A. D. (1974). Paleocurrent analysis of alluvial sediments: A discussion of directional variance and vector magnitude. *Journal of Sedimentary Research*, *44*(4), 1174–1185.

Moodie, A. J., & Nittrouer, J. A. (2021). Optimized river diversion scenarios promote sustainability of urbanized deltas. *Proceedings of the National Academy of Sciences*, *118*(27), e2101649118. https://doi.org/10.1073/pnas.2101649118

Nagel, G. W., de Moraes Novo, E. M. L., Martins, V. S., Campos-Silva, J. V., Barbosa, C. C. F., & Bonnet, M. P. (2022). Impacts of meander migration on the Amazon riverine communities using Landsat time series and cloud computing. *Science of the Total Environment*, *806*, 150449. https://doi.org/10.1016/j.scitotenv.2021.150449

Naito, K., & Parker, G. (2019). Can bankfull discharge and bankfull channel characteristics of an alluvial meandering river be cospecified from a flow duration curve? *Journal of Geophysical Research: Earth Surface*, *124*(10), 2381–2401. https://doi.org/10.1029/2018jf004971

Nanson, G. C., & Hickin, E. J. (1986). A statistical analysis of bank erosion and channel migration in western Canada. *Geological Society of America Bulletin*, *97*(4), 497–504. https://doi.org/10.1130/0016-7606(1986)97<497:asaobe>2.0.co;2

Nogueira, J., Lecuona, A., & Rodríguez, P. A. (2001). Identification of a new source of peak locking, analysis and its removal in conventional and super-resolution PIV techniques. *Experiments in Fluids*, *30*(3), 309–316. https://doi.org/10.1007/s003480000179

Paola, C., Heller, P. L., & Angevine, C. L. (1992). The large-scale dynamics of grain-size variation in alluvial basins, 1: Theory. *Basin Research*, *4*(2), 73–90. https://doi.org/10.1111/j.1365-2117.1992.tb00145.x

Passalacqua, P., Giosan, L., Goodbred, S., & Overeem, I. (2021). Stable ≠ sustainable: Delta dynamics versus the human need for stability. *Earth's Future*, *9*(7), e2021EF002121. https://doi.org/10.1029/2021ef002121

Peixoto, J. M. A., Nelson, B. W., & Wittmann, F. (2009). Spatial and temporal dynamics of river channel migration and vegetation in central Amazonian white-water floodplains by remote-sensing techniques. *Remote Sensing of Environment*, *113*(10), 2258–2266. https://doi.org/10.1016/j.rse.2009.06.015

Perkins, S., Edlund, K., Esch-Mosher, D., Eads, D., Harvey, N., & Brumby, S. (2005). Genie pro: Robust image classification using shape, texture, and spectral information. In *Algorithms and technologies for multispectral, hyperspectral, and ultraspectral imagery XI* (Vol. 5806, p. 139). SPIE. https://doi.org/10.1117/12.604519

Repasch, M., Scheingross, J. S., Hovius, N., Lupker, M., Wittmann, H., Haghipour, N., et al. (2021). Fluvial organic carbon cycling regulated by sediment transit time and mineral protection. *Nature Geoscience*, *14*(11), 842–848. https://doi.org/10.1038/s41561-021-00845-7

Rowland, J., Shelef, E., Pope, P. A., Muss, J., Gangodagamage, C., Brumby, S. P., & Wilson, C. J. (2016). A morphology independent methodology for quantifying plan view river change and characteristics from remotely sensed imagery. *Remote Sensing of Environment*, *184*, 212–228. https://doi.org/10.1016/j.rse.2016.07.005

Rowland, J., Stauffer, S., & Schwenk, J. (2019). Pan-arctic river bank erosion and accretion, and planform metrics measured over intervals ranging from 1973 to 2016. https://doi.org/10.15485/1571527

Scarano, F., & Riethmuller, M. L. (1999). Iterative multigrid approach in PIV image processing with discrete window offset. *Experiments in Fluids*, *26*(6), 513–523. https://doi.org/10.1007/s003480050318

Scheingross, J. S., Repasch, M. N., Hovius, N., Sachse, D., Lupker, M., Fuchs, M., et al. (2021). The fate of fluvially-deposited organic carbon during transient floodplain storage. *Earth and Planetary Science Letters*, *561*, 116822. https://doi.org/10.1016/j.epsl.2021.116822

Schwenk, J., & Foufoula-Georgiou, E. (2016). Meander cutoffs nonlocally accelerate upstream and downstream migration and channel widening. *Geophysical Research Letters*, *43*(24), 12437–12445. https://doi.org/10.1002/2016GL071670

Schwenk, J., & Hariharan, J. (2021). RivGraph: Automatic extraction and analysis of river and delta channel network topology. *Journal of Open Source Software*, *6*(59), 2952. https://doi.org/10.21105/joss.02952

Schwenk, J., Khandelwal, A., Fratkin, M., Kumar, V., & Foufoula-Georgiou, E. (2017). High spatiotemporal resolution of river planform dynamics from Landsat: The rivMAP toolbox and results from the Ucayali river. *Earth and Space Science*, *4*(2), 46–75. https://doi.org/10.1002/2016EA000196

Sciacchitano, A. (2019). Uncertainty quantification in particle image velocimetry. *Measurement Science and Technology*, *30*(9), 092001. https://doi.org/10.1088/1361-6501/ab1db8

Singh, A., Thomsen, K. J., Sinha, R., Buylaert, J. P., Carter, A., Mark, D. F., et al. (2017). Counter-intuitive influence of Himalayan river morphodynamics on Indus Civilisation urban settlements. *Nature Communications*, *8*(1), 1617. https://doi.org/10.1038/s41467-017-01643-9

Slingerland, R., & Smith, N. D. (2004). River avulsions and their deposits. *Annual Review of Earth and Planetary Sciences*, *32*(1), 257–285. https://doi.org/10.1146/annurev.earth.32.101802.120201

Sun, T., Meakin, P., Jøssang, T., & Schwarz, K. (1996). A simulation model for meandering rivers. *Water Resources Research*, *32*(9), 2937–2954. https://doi.org/10.1029/96WR00998

Sylvester, Z., Durkin, P., & Covault, J. A. (2019). High curvatures drive river meandering. *Geology*, *47*(3), 263–266. https://doi.org/10.1130/G45608.1

Tal, M., Gran, K., Murray, A. B., Paola, C., & Hicks, D. M. (2013). Riparian vegetation as a primary control on channel characteristics in multi-thread rivers. In *Riparian vegetation and fluvial geomorphology* (pp. 43–58). https://doi.org/10.1029/008WSA04

Thakur, P. K., Laha, C., & Aggarwal, S. P. (2012). River bank erosion hazard study of river Ganga, upstream of Farakka barrage using remote sensing and GIS. *Natural Hazards*, *61*(3), 967–987. https://doi.org/10.1007/s11069-011-9944-z

Thielicke, W., & Stamhuis, E. J. (2014). PIVlab–Towards user-friendly, affordable and accurate digital particle image velocimetry in MATLAB. *Journal of Open Research Software*, *2*(1), e30. https://doi.org/10.5334/jors.bl

Torres, M. A., Limaye, A. B., Ganti, V., Lamb, M. P., West, A. J., & Fischer, W. W. (2017). Model predictions of long-lived storage of organic carbon in river deposits. *Earth Surface Dynamics*, *5*(4), 711–730. https://doi.org/10.5194/esurf-2017-29

Valenza, J. M., Edmonds, D. A., & Weissmann, G. S. (2022). Quantifying River avulsion activity from satellite remote sensing: Implications for how avulsions contribute to floodplain stratigraphy in foreland basins. *Journal of Sedimentary Research*, *92*(6), 487–502. https://doi.org/10.2110/jsr.2021.038

Ward, J. V., & Stanford, J. A. (1995). Ecological connectivity in alluvial river ecosystems and its disruption by flow regulation. *Regulated Rivers: Research & Management*, *11*(1), 105–119. https://doi.org/10.1002/rrr.3450110109

Westerweel, J. (1997). Fundamentals of digital particle image velocimetry. *Measurement Science and Technology*, *8*(12), 1379–1392. https://doi.org/10.1088/0957-0233/8/12/002

Wickert, A. D., Martin, J. M., Tal, M., Kim, W., Sheets, B., & Paola, C. (2013). River channel lateral mobility: Metrics, time scales, and controls. *Journal of Geophysical Research: Earth Surface*, *118*(2), 396–412. https://doi.org/10.1029/2012JF002386

Willenbring, J. K., Codilean, A. T., & McElroy, B. (2013). Earth is (mostly) flat: Apportionment of the flux of continental sediment over millennial time scales. *Geology*, *41*(3), 343–346. https://doi.org/10.1130/g33918.1

Wilson, C. A., & Goodbred, S. L. (2015). Construction and maintenance of the Ganges-Brahmaputra-Meghna delta: Linking process, morphology, and stratigraphy. *Annual Review of Marine Science*, *7*(1), 67–88. https://doi.org/10.1146/annurev-marine-010213-135032

Wohl, E., Angermeier, P. L., Bledsoe, B., Kondolf, G. M., MacDonnell, L., Merritt, D. M., et al. (2005). River restoration. *Water Resources Research*, *41*(10), 1–12. https://doi.org/10.1029/2005WR003985

Yamazaki, D., Ikeshima, D., Sosa, J., Bates, P. D., Allen, G. H., & Pavelsky, T. M. (2019). MERIT hydro: A high-resolution global hydrography map based on latest topography dataset. *Water Resources Research*, *55*(6), 5053–5073. https://doi.org/10.1029/2019WR024873

Yang, X., Pavelsky, T. M., Allen, G. H., & Donchyts, G. (2020). RivWidthCloud: An automated Google Earth engine algorithm for river width extraction from remotely sensed imagery. *IEEE Geoscience and Remote Sensing Letters*, *17*(2), 217–221. https://doi.org/10.1109/LGRS.2019.2920225

Erratum

In the originally published version of this article, the author contribution section omitted the contributions of corresponding author "Austin J. Chadwick." Dr. Chadwick has been attributed to Conceptualization, Formal analysis, Investigation, Methodology, Software, Validation, Visualization, Writing – original draft, and Writing – review & editing. The errors have been corrected, and this may be considered the authoritative version of record.